Tracking Extended Objects with Basic Parametric Shapes using Deformable Superellipses

Tim Baur, Patrick Hoher, and Johannes Reuter
Institute of System Dynamics (ISD)
University of Applied Sciences Konstanz (HTWG)
Konstanz, Germany
{tbaur,phoher,jreuter}@htwg-konstanz.de

Uwe D. Hanebeck
Intelligent Sensor-Actuator-Systems Laboratory (ISAS)
Karlsruhe Institute of Technology (KIT)
Karlsruhe, Germany
uwe.hanebeck@kit.edu

***Abstract*—In extended object tracking, basic parametric shapes such as ellipses and rectangles or non-parametric shape representations such as Fourier series or Gaussian processes can be utilized as shape priors. However, flexible non-parametric shape representations can be disproportionately detailed and computationally intensive for many applications. Therefore, we propose to adopt deformable superellipses for a low-dimensional and flexible representation of basic parametric shapes in this paper. We present a measurement model in 2D space that can cope with boundary and interior measurements simultaneously by recursively estimating an artificial noise variance for interior measurements. We investigate and compare the model in a simulated and real-world maritime scenario with the result that the combination of deformable superellipses and artificial measurement noise estimation performs better than state-of-the-art methods.**

***Index Terms*—Extended object tracking, 2D space, superellipse, boundary-interior measurements.**

I. Introduction

With ever-increasing resolutions of RADAR, LiDAR, and other sensor devices, extended object tracking (EOT) [1] became an essential part of many surveillance systems such as advanced driver assistance in automotive or maritime applications. Due to the high resolution of the aforementioned sensors, multiple sensor cells detect the same target, which results in a few to thousands of measurements per time step, depending on the sensor device and distance of the sensor to the target. The goal of EOT is thus to process measurements in an extended object measurement model. This model then maps the space of system states, comprising kinematic and extent state, to the measurement space.

An essential part of deriving a measurement model in EOT is the definition of the shape class to be used within the measurement model. If the shape class of the target to be tracked is known a priori, it can be used directly in the measurement model. In 2D space, the most popular basic parametric shape to be applied in EOT is an ellipse. Hence, many elliptical EOT measurement models have been proposed in the past years. The most well-known is the random matrices (RM) approach [2]. In the RM framework, measurements are assumed to be scattered normally distributed around the center of the target. This assumption results in a robust, efficient, and easy-to-implement algorithm that has been used in many applications and improved in various papers [3]–[5]. Another approach that seeks to estimate an elliptical extent is the random hypersurface model (RHM) proposed in [6]. In the RHM approach, measurements are assumed to be scattered from a scaled version of the boundary. Hence, the scaling factor is modeled as a user-definable random variable, which makes the RHM approach more flexible than the RM approach. Further elliptical models can be found in [7], [8]. Other basic parametric shapes in 2D space are rectangles, especially applied to describe the extent of vehicles in automotive applications. Popular models for rectangular EOT can be found in [9], [10]. If no prior knowledge of the shape class of the target is available, non-parametric shape-tracking procedures can be applied. In 2D space, the RHM framework can be utilized to track star-convex shapes. The shape can then be represented using Fourier series [11], Gaussian processes [12], or lengths of radial segments [13].

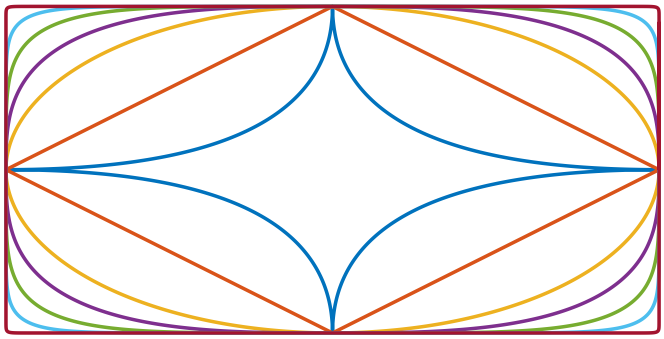

Figure 1: Superellipses with squareness parameters $\underline{\varepsilon} = [0.5, 1, 2, 3, 5, 10, 100]^T$. The red square has $\varepsilon = 100$.

In summary, when designing an EOT measurement model, there is a choice between basic parametric shape representations and flexible non-parametric shape-tracking procedures. When using parametric shapes, the reason is often the lower dimensionality of the extent state, which is contained in the system state, and the resulting lower computational effort required for estimation. If no prior knowledge of the shape class of the target is available, the designer is however forced to use non-parametric shape-tracking procedures or to apply

multiple model approaches [3], [14] that can distinguish between basic parametric shapes. In this paper, we close the gap between using an efficient parametric shape measurement model compared to non-parametric shape-tracking procedures. Therefore, we propose to use deformable superellipses as shape representations. Superellipses are a class of closed curves that contain a rhombus, an ellipse, and a rectangle as special cases [15]. An illustration of different superellipse shapes can be seen in Fig. 1. Superellipses have been applied for state estimation of articulated extended objects in [16] and for segmentation and shape fitting in [17]. However, both approaches propose optimization-based algorithms that do not take object dynamics into account compared to the Bayesian tracking filters that we use.

A problem in EOT that arises in real-world applications is related to the assumptions that are made for the measurement source distributions in the aforementioned models. In [2], [7], specific assumptions about the measurement source spatial distributions are made. In the RHM approach [6], [11], the distribution of the scaling factor has to be specified before running the algorithm. Finally, in models such as [10], the measurements are assumed to originate exclusively from the boundary of the target. However, if these assumptions do not hold, an estimation bias is introduced. It has been shown in [18], that often a mixture of boundary-interior measurements are present, for example, if 3D measurements are projected to the 2D horizontal plane. In [19], the measurement source distribution is modeled as truncated Gaussian processing measurements either gathered from the boundary or the interior of the target. In this paper, we extend the approach presented in [18] and recursively learn an artificial measurement noise variance for measurements from the interior of the target.

The main contributions of the paper can be summarized as follows:

- We present a measurement model in 2D space to estimate a deformable superellipse shape for mixed boundary-interior measurements.
- We present an approach to recursively learn an artificial measurement noise variance to efficiently process measurements from the interior of the target.
- We investigate our approach in a comprehensive comparison to fixed parametric shape models and flexible non-parametric shape-tracking procedures in a simulated and real-world scenario.

In addition, we present an easy-to-implement and efficient approach to state estimation with interval constraints suitable for superellipse extent parameters.

II. Problem Formulation

In EOT, the task is to estimate the extent or shape of the target simultaneously with the kinematic state at each time step k using the measurement set

$$\mathcal{Y}_k = \left\{ \underline{y}_{k,l} \right\}_{l=1}^{n_k} . \tag{1}$$

The measurements $\underline{y}_{k,l}$ are spatially distributed providing information about the location, extent, and shape of the target. The number of measurements $n_k \geq 1$ can vary over time. In this paper, we present a measurement model in 2D space for $\underline{y}_{k,l} \in \mathbb{R}^2$. Extensions to process 3D measurements are left for future work.

The system state to be estimated is described as

$$\underline{x}_k = \left[\underline{x}_{\text{kin}_k}^T, \underline{x}_{\text{ext}_k}^T \right]^T \tag{2}$$

with the kinematic state $\underline{x}_{\text{kin}_k} = \left[\underline{m}_k^T, \phi_k, \underline{x}_{\text{vel}_k}^T \right]^T$ comprising the position $\underline{m}_k \in \mathbb{R}^2$, the orientation ϕ_k, and the velocity components $\underline{x}_{\text{vel}_k}$. The orientation ϕ_k is modeled to be aligned with the velocity vector. The extent state $\underline{x}_{\text{ext}_k}$ will be discussed in Sec. IV.

In this paper, we apply the measurement source model

$$\underline{y}_{k,l} = \underline{z}_{k,l} + \underline{v}_{k,l} \tag{3}$$

with measurement source $\underline{z}_{k,l}$ and white Gaussian zero-mean noise term $\underline{v}_{k,l} \sim \mathcal{N}\left(\underline{0}, \mathbf{C}_{\underline{v}}\right)$ as measurement generating process. In this approach, the measurement is assumed to be a noise-corrupted observation of a point located on the target. Since the measurement source $\underline{z}_{k,l}$ is typically unknown, we are faced with the well-known measurement source association problem [1]. In Sec. IV and Sec. V, we present an approach to solve the measurement source association problem for mixed boundary-interior measurements using a greedy association model together with a recursive noise estimation procedure.

III. Superellipses

Superellipses, also known as Lamé curves, are a special class of curves that give a compact representation of basic parametric 2D shapes [15], [20]. Implicitly, a superellipse can be given as the set

$$\begin{aligned} \mathcal{S}(\underline{p}, a, b, \varepsilon) = \Bigg\{ \underline{p} \in \mathbf{R}^2 \Bigg| \, & F(p_x, p_y, a, b, \varepsilon) \\ & = \left| \frac{p_x}{a} \right|^{\varepsilon} + \left| \frac{p_y}{b} \right|^{\varepsilon} - 1 = 0 \Bigg\} \end{aligned} \tag{4}$$

with $\underline{p} = [p_x, p_y]^T$, and $a, b > 0$ being the major and minor semi-axes defining the extent of the superellipse, and the squareness parameter ε the shape. The implicit representation (4) describes the closed curve centered at the origin and aligned with the coordinate axes. The squareness parameter $\varepsilon \geq 0$ defines the shape of the curve. With $0 \leq \varepsilon < 1$, the superellipse describes pinched rhombus shapes with a cross at the limit case of $\varepsilon = 0$. At $\varepsilon = 1$ or $\varepsilon = 2$, the shape results in a rhombus or an ellipse, respectively. With $\varepsilon > 2$, the superellipse shape gives a rectangle with rounded corners and an actual rectangle at the limit case of $\lim_{\varepsilon \to \infty}$. An illustration of the superellipse shape with respect to the squareness parameter ε can be seen in Fig. 1.

Another representation of the superellipse shape can be given explicitly using the parameter $0 \leq \theta < 2\pi$ as

$$p_x(\theta) = a \, \text{sign}\big(\cos(\theta)\big) \, |\cos(\theta)|^{\frac{2}{\varepsilon}} , \tag{5a}$$

$$p_y(\theta) = b \, \text{sign}\big(\sin(\theta)\big) \, |\sin(\theta)|^{\frac{2}{\varepsilon}} , \tag{5b}$$

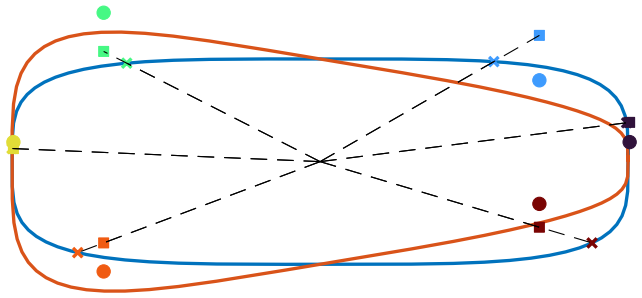

Figure 2: Tapered superellipse and measurement source association. Squareness parameter $\varepsilon = 4$. Tapering parameter $\underline{t}_y = -0.5$. Measurements as circles, inverse tapered measurements as squares, and measurement sources on non-tapered shape as crosses. Related items are displayed in the same color.

where sign() represents the signum function. The explicit representation can be used to plot the superellipse.

In addition to the squareness transformation, a tapering transformation [21] for each axis can be introduced to be able to taper the shape in each direction. In doing so, shapes such as triangles and trapezoids can also be represented using superellipses. A tapering transformation $\mathcal{T}\left(\underline{p}\right)$ can be given as

$$\mathcal{T}\left(\underline{p}\right) = \left[\left(t_x \frac{p_y}{b} + 1\right) p_x \,,\, \left(t_y \frac{p_x}{a} + 1\right) p_y\right]^T \tag{6}$$

using the tapering coefficients $t_x, t_y \in [-1, 1]$. An inverse tapering transformation will be denoted as $\mathcal{T}^{-1}$ in the following. A tapered superellipse can be seen in Fig. 2.

IV. Measurement Model

In this section, we present the measurement model for tracking targets with a superellipse shape using measurements in 2D space. We present the measurement model for measurements stemming from the target boundary as measurements from the interior are processed using the recursively estimated artificial measurement noise variance presented in Sec. V.

A. Preliminary considerations

Our model is not restricted to specific applications or sensors. When exclusively measurements from the boundary are expected, the model presented in this section can directly be used. When mixed boundary-interior measurements are expected, e.g., when projecting 3D LiDAR data to the 2D horizontal plane, the recursive measurement noise estimation can be added to the update step. In the measurement model derivation, we omit the time and measurement indexes k and l for the sake of simplicity. Since measurements are assumed to be mutually independent, the measurement model can be applied to each measurement individually. Details on the implementation are given in Sec. VI.

The extent state in (2) can be defined individually depending on the desired flexibility of the model. More and more parameters can be added to achieve an increasingly flexible model. Following, three possibilities for defining the extent state are given:

- $\underline{x}_{\text{ext}} = [a, b]^T$: The least flexible model in 2D space estimates only the extent of a specific superellipse with a fixed squareness parameter ε. However, we want to highlight that this option can be very powerful as well if prior knowledge of the class of the target shape is available. With $t_x = t_y = 0$, which is equal to no tapering transformation, and $\varepsilon = 10$ for example, a rectangle with rounded corners similar to [10] can be described.
- $\underline{x}_{\text{ext}} = [a, b, \varepsilon]^T$: By adding the squareness parameter ε to the extent state, scaled versions of the shapes from Fig. 1 can be estimated.
- $\underline{x}_{\text{ext}} = [a, b, \varepsilon, t_x, t_y]^T$: By also adding the tapering coefficients t_x, t_y to the extent state, tapering deformations, as can be seen in Fig. 2, of the superellipse shape can be estimated.

In our investigation in Sec. VII we set the extent state as comprising the semi-axes a and b and the squareness coefficient ε together with the tapering coefficient t_y to allow tapering deformations in the y-axis. In local target coordinates, omitting the tapering coefficient t_x introduces a line of symmetry in x-direction, which is aligned to the direction of movement in sensor coordinates. This restriction is reasonable for many targets in various tracking scenarios.

In this paper, we describe the boundary of the superellipse shape in local target coordinates as the set (4). Ideally, this implicit representation could be used in a measurement equation similar to [22]. However, investigations already showed that the nonlinear nature of the squareness parameter ε makes parameter estimation very difficult [15]. This result was supported by an own implementation of an implicit measurement equation, which also showed very unstable estimation results. Therefore, we derived an explicit measurement equation.

B. Measurement equation

To derive an explicit measurement equation, the measurement source model (3) can be applied. However, the unknown measurement source has to be approximated. We approximate the measurement source as the intersection of the boundary and the connecting line between the center of the superellipse and the inverse tapered measurement. In contrast to the orthogonal projection, this approximation enables an efficient analytical calculation of the measurement source. An illustration of the association scheme is given in Fig. 2. To be able to predict the measurement source, the first step is to transform the measurement to local target coordinates as

$$\underline{\tilde{y}} = \mathbf{R}_\phi^{-1} \left(\underline{y} - \underline{m}\right) \tag{7}$$

using the rotation matrix $\mathbf{R}_\phi$. If a tapering transformation is applied, the next step is to inversely taper the measurement in local coordinates. The inverse tapering transformation for measurements in local coordinates can be given as

$$\underline{\tilde{y}} := \mathcal{T}^{-1}\left(\underline{\tilde{y}}\right) = \left[\frac{\tilde{y}_x}{t_x \frac{\tilde{y}_y}{b} + 1} \,,\, \frac{\tilde{y}_y}{t_y \frac{\tilde{y}_x}{a} + 1}\right]^T \tag{8}$$

with $\underline{\tilde{y}} = [\tilde{y}_x, \tilde{y}_y]^T$. Given the inverse tapered measurement in local coordinates $\underline{\tilde{y}}$, the implicit superellipse representation (4)

and the association scheme described before, the intersection point $\tilde{\underline{z}}\left(\tilde{\underline{y}}\right) = \left[\tilde{x}_s\left(\tilde{\underline{y}}\right), \tilde{y}_s\left(\tilde{\underline{y}}\right)\right]^T$ in local coordinates can then analytically be given as

$$\tilde{x}_s\left(\tilde{\underline{y}}\right) = \operatorname{sign}\left(\tilde{y}_x\right)\left(|a|^{-\varepsilon} + \left|\frac{\tilde{y}_y}{b\,\tilde{y}_x}\right|^{\varepsilon}\right)^{-\frac{1}{\varepsilon}}, \tag{9a}$$

$$\tilde{y}_s\left(\tilde{\underline{y}}\right) = \tilde{x}_s\left(\tilde{\underline{y}}\right)\frac{\tilde{y}_y}{\tilde{y}_x} \tag{9b}$$

with $\tilde{\underline{y}} = [\tilde{y}_x, \tilde{y}_y]^T$. If only one or no tapering transformation is applied, the intersection point can be calculated using the measurement in local coordinates directly. Given the inverse tapered measurement source in local coordinates $\tilde{\underline{z}}\left(\tilde{\underline{y}}\right)$ and the inverse tapered measurement in local coordinates $\tilde{\underline{y}}$, a measurement equation in local coordinates for 2D boundary measurements can be formulated as

$$\begin{aligned}\bar{\underline{y}} &= h\left(\underline{x}, \mathcal{T}^{-1}(\tilde{\underline{y}})\right) + \underline{v} \\ &= \tilde{\underline{z}}\left(\mathcal{T}^{-1}(\tilde{\underline{y}})\right) - \mathcal{T}^{-1}\left(\tilde{\underline{y}}\right) + \underline{v} \\ &= \tilde{\underline{z}}\left(\tilde{\underline{y}}\right) - \tilde{\underline{y}} + \underline{v}\end{aligned} \tag{10}$$

with $\bar{\underline{y}}$ being the innovation error. Due to the nonlinearities in the measurement equation, a nonlinear Kalman filter must be applied for state estimation. Details are given in Sec. VI.

V. Recursive Noise Estimation

In the previous section, we presented a measurement equation to process measurements gathered from the boundary of the target. In real-world applications, however, measurements often occur in a mixed boundary-interior measurement fashion. In [18], the spatial distribution of LiDAR measurements is investigated by calculating the distribution of an RHM scaling parameter under an assumed radial measurement source association for multiple instances of real-world targets. It is seen that many measurements stem from the boundary of the target and also that the assumption of a uniformly distributed squared scaling factor, which is often assumed in RHMs, is not valid for real-world data. The solution proposed in [18] is to use a measurement equation for boundary measurements and to heuristically calculate an asymmetric measurement noise variance for measurements lying inside the predicted target boundary. In this paper, we adopt the approach presented in [18], but recursively estimate the variance of an artificial measurement noise for measurements that lie within the boundary, rather than heuristically setting a specific value.

Determining whether a measurement lies within the predicted boundary can efficiently be calculated using the implicit superellipse representation $F(p_x, p_y, a, b, \varepsilon)$ in (4) that is also termed "inside-outside" function [20]. Using the inverse tapered measurement in local coordinates $\tilde{\underline{y}}$ that can be calculated with the predicted system state $\underline{x}_{k|k-1}$, the "inside-outside" information can approximately well be generated as

$$F(\tilde{y}_x, \tilde{y}_y, a_{k|k-1}, b_{k|k-1}, \varepsilon_{k|k-1}) \begin{cases} > 0: & \text{outside} \\ = 0: & \text{boundary} \\ < 0: & \text{inside} \end{cases}$$

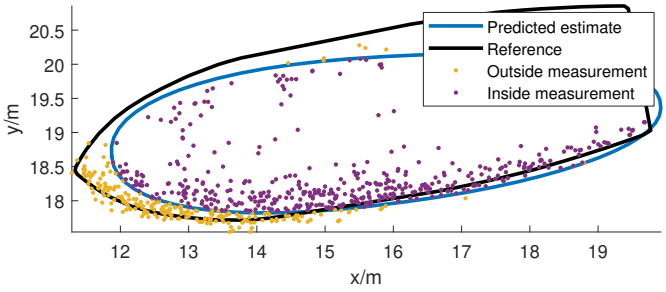

Figure 3: Illustration of the "inside-outside" information.

for a low measurement noise. For measurements inside the boundary, we then calculate the artificial measurement noise variance. An illustration of the "inside-outside" information at a specific time step can be seen in Fig. 3. A discussion about incorrectly assigned measurements and the effects on the state estimate can be found in [18].

For the artificial measurement noise, we assume isotropy in both directions and that the measurements inside the boundary stem from the same measurement-generating process with a single measurement noise variance rather than a heuristic variance for each measurement. Also, we assume the artificial measurement noise to have zero mean. Given the innovation error $\bar{\underline{y}}$ for every time step until k, the artificial measurement noise variance can be given as

$$\hat{\sigma}_k^{(i)} = \frac{1}{2\,\Sigma_k^{(i)}} \sum_{m=1}^{k} \sum_{l=1}^{n_k^{(i)}} \bar{y}_{x_{m,l}}^{(i)2} + \bar{y}_{y_{m,l}}^{(i)2} \tag{11}$$

with $\bar{\underline{y}}^{(i)} = \left[\bar{y}_x^{(i)}, \bar{y}_y^{(i)}\right]^T$, using the standard maximum likelihood variance estimator. In this equation, the superscript (i) represents quantities of measurements inside the boundary. Furthermore, the notation $\Sigma_k^{(i)} := \sum_{l=1}^{k} n_l^{(i)}$ indicates the number of measurements inside the boundary from time step 1 to k summed up. Given the variance estimator (11) for the measurement sets up to time step k, a recursive estimator can be derived as

$$\hat{\sigma}_k^{(i)} = \frac{1}{1 + \frac{2\,n_k^{(i)}}{2\,\Sigma_{k-1}^{(i)}}}\,\hat{\sigma}_{k-1}^{(i)} + \frac{1}{2\,\Sigma_k^{(i)}} \sum_{l=1}^{n_k^{(i)}} \bar{y}_{x_{k,l}}^{(i)2} + \bar{y}_{y_{k,l}}^{(i)2}. \tag{12}$$

In this recursive estimator, measurements from the first and the last time step equally contribute to the variance estimation. This is, however, not preferable as the distribution can vary over time, e.g., when the viewing angle of the target changes. Therefore, we introduce a forgetting factor τ replacing $2\Sigma_{k-1}^{(i)}$ similar to [23] that can be interpreted as the number of measurements from the past that still contribute to the recursive variance estimation. The final recursive estimator of the artificial measurement noise is then given as

$$\hat{\sigma}_k^{(i)} = \frac{1}{1 + \frac{2\,n_k^{(i)}}{\tau}}\,\hat{\sigma}_{k-1}^{(i)} + \frac{1}{\tau + 2\,n_k^{(i)}} \sum_{l=1}^{n_k^{(i)}} \bar{y}_{x_{k,l}}^{(i)2} + \bar{y}_{y_{k,l}}^{(i)2}. \tag{13}$$

In our investigations in Sec. VII we use a forgetting factor of $\tau = 200$ for every scenario. In the update step of the Kalman filter, the measurement noise covariance matrix can then be calculated as

$$\mathbf{C}_{\underline{v}_{k,l}} = \begin{cases} \text{diag}\left(\hat{\sigma}_k^{(i)}, \hat{\sigma}_k^{(i)}\right) & \text{if inside} \\ \text{diag}(\sigma_{\underline{v}}^2, \sigma_{\underline{v}}^2) & \text{else} \end{cases} \tag{14}$$

with $\sigma_{\underline{v}}^2$ being the sensor measurement noise variance that can be taken from the sensor data sheet. In future work, we will discuss and investigate the assumptions of isotropic noise and a zero mean value in more detail.

VI. Implementation Details

The implementation of the model presented in the previous sections can be performed using linear regression Kalman filters such as the UKF and the S2KF [24], [25]. Both implementations are compared in the results in Sec. VII. In this section, additional information on implementing the superellipse-shaped extended object measurement model is given.

A. Single time step measurement processing

As described in Sec. II, measurements from a single time step are mutually independent and can be processed in a sequential measurement update as was done in [7]. Another option would be to process measurements in a stacked measurement update as presented in [26]. The advantage of a sequential measurement update is the lower computational effort resulting from the inversion of a small innovation covariance matrix in the Kalman filter update. The disadvantage of a sequential measurement update is that the final state estimate strongly depends on the order in which the measurements are processed due to the inherent linearization in the Kalman filter update. On the other hand, the size of the innovation covariance matrix and the resulting computation time in a stacked measurement update depends on the number of measurements recorded in a single time step. The final state estimate is, however, reproducible since all measurements are processed at once. To combine the advantages and disadvantages of both approaches, we propose to process a specific amount of measurements in a stacked measurement implementation and repeat this procedure in a sequential update until every measurement is handled. In our implementations, we always process 10 randomly selected measurements in a single stacked measurement update.

B. State interval constraints

One issue with many EOT approaches is the fact that extent or shape parameters are often subject to interval constraints. In our superellipse model, the semi-axes a and b should be within the interval $a, b \in (0, \infty]$ to prevent the extension from becoming negative. The squareness parameter ε produces concave shapes for $\varepsilon < 1$ and convex shapes for the opposite interval. Concave shapes are not preferable for EOT. Therefore, we would like to have the squareness parameter within the interval $\varepsilon \in [1, \infty]$. Finally, the tapering coefficients should be within the interval $t_x, t_y \in [-1, 1]$ since higher or lower values would produce loops in the shape which are not preferable.

In standard Kalman filtering, interval constraints can not be introduced, since a Gaussian distribution, which is applied as state distribution, has an unbounded domain. In the literature, several approaches can be found to modify nonlinear Kalman filtering to be able to handle state interval constraints. In [27], for example, multiple procedures for the UKF can be found. In this paper, we use a simple approach that allows the Kalman filter to estimate unconstrained state variables and also provides constrained extent parameter estimates. We define several monotonically increasing state transformation functions that have an unbounded domain and a bounded codomain. The unbounded state variables are then transformed through these functions before using the parameters in the filter processing or before using the filter estimate in an evaluation. By applying monotonically increasing transformation functions, we ensure a unique assignment between constrained and unconstrained variables. This procedure results in a very efficient and effective method to handle state interval constraints without changing the process of the Kalman filter.

Since we have three different interval constraints in our superellipse model, we also need three different transformation functions $\mathfrak{t}$ to transform the respective extent parameters to a bounded codomain. The bounds for the tapering coefficients t_x, t_y can be achieved using a modified arctangent function. The transformation function

$$\mathfrak{t}_1(x) = \frac{2}{\pi} \arctan(x) \tag{15}$$

generates bounded tapering coefficients $t_x^{(b)}, t_y^{(b)}$ within the interval $t_x^{(b)}, t_y^{(b)} \in [-1, 1]$. The semi-axes a and b are restricted to nonzero values. These constraints can be achieved using the piecewise continuous function

$$\mathfrak{t}_2(x) = \begin{cases} \exp(x) & x < 0 \\ x + 1 & \text{else} \end{cases} \tag{16}$$

that generates bounded semi-axes $a^{(b)}, b^{(b)}$ within the interval $a^{(b)}, b^{(b)} \in (0, \infty]$. Please note, that the transformation function $\mathfrak{t}_2(x)$ linearly increases for $x > 0$, which simplifies state estimation. In addition, the function is differentiable and could therefore also be used in an extended Kalman filter implementation. Finally, the squareness parameter ε is restricted to values greater than one. This constraint can be achieved by simply shifting $\mathfrak{t}_2(x)$ as

$$\mathfrak{t}_3(x) = \mathfrak{t}_2(x) + 1, \tag{17}$$

which generates a bounded squareness parameter $\varepsilon^{(b)}$ within the interval $\varepsilon^{(b)} \in [1, \infty]$. Please note, that this transformation function has the same advantages as $\mathfrak{t}_2(x)$.

VII. Results

In this section, we compare our approach to several other state-of-the-art models in a comprehensive simulated and real-world investigation. In both scenarios, we investigate the superellipse measurement model with recursive noise estimation

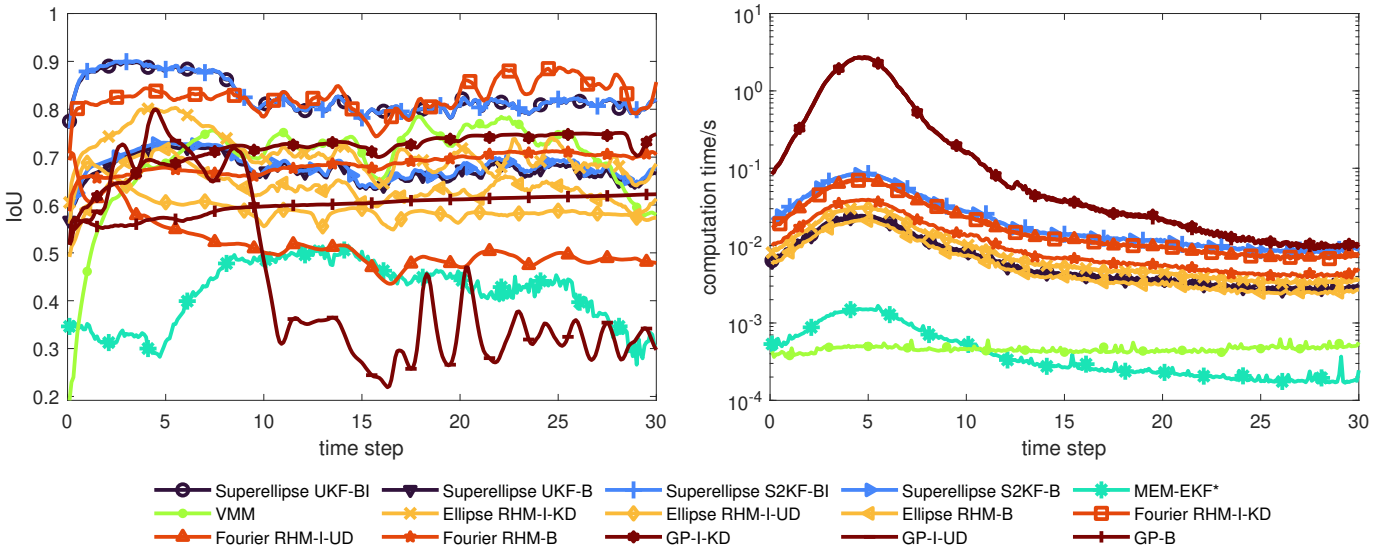

Figure 4: IoU and computation time results of the simulated scenario.

for mixed boundary-interior (BI) measurements using an UKF and an S2KF implementation. We compare our model with the superellipse model, where only boundary measurements are assumed for the entire measurement set without discarding any measurements, using also an UKF (UKF-B) and an S2KF (S2KF-B) implementation. The S2KF implementations utilize 10 samples per dimension. Additionally, we apply the multiplicative error model (MEM-EKF*) [7], the virtual measurement model (VMM) approach [3], the ellipse and star-convex RHMs [6], [11], and the Gaussian process (GP) model [12] as comparison. The star-convex shape in the RHM implementation is represented using 7 shape coefficients for the Fourier series expansion. For the GP model we use the same parameters as in [12], except for the length scale, which we set to $l = \pi/2$ to favor smoother shapes. Also, we use 20 basis angles in the GP system state. The RHMs are all implemented using an UKF, the GP, and MEM-EKF* models using an EKF as proposed by the authors. To get a better intuition on the impact of the scaling factor in the RHM, we also compare several specifics of the RHM approach. First, we apply implementations of both RHMs where only boundary measurements are assumed (RHM-B). Furthermore, we compare implementations of the RHM models assuming interior measurements with a known distribution (I-KD) of the scaling factor with implementations where we have an unknown spatial distribution of the interior measurements (I-UD). The same investigations are provided for the GP model [12]. In the case of an unknown scaling factor distribution, we assume a uniformly distributed squared scaling factor in the interval $[0, 1]$ as the best guess.

Both scenarios, the one with simulated data and the one with real-world data, were already used and described in [28]. Also in both scenarios, measurements from a 3D LiDAR sensor [29] are recorded in a maritime scenario. Measurements are always taken from our research vessel "Solgenia" at HTWG Konstanz. For the simulated scenario, we utilized a CAD model of the vessel. Since we propose a measurement model for 2D data in this paper, we project the measurements onto the 2D horizontal plane, which results in mixed boundary-interior measurements. We initialize every filter using the first measurement set as already presented in [28].

In both investigations, we apply a coordinated turn model [30] as motion model. We compare the measurement model performances using the intersection over union (IoU) measure [31]. The IoU measure is given as

$$\text{IoU} = \frac{\text{area}(S_t \cap S_e)}{\text{area}(S_t \cup S_e)} \tag{18}$$

with the true shape S_t and the estimated shape S_e. In 2D space, an arbitrary shape can be approximated using a polygonal chain. Intersection shapes, union shapes, and respective areas can then easily be calculated. We extract the reference shape S_t as 2D convex hull from the CAD model. Additionally, we measure the computation time. Every calculation was conducted using MATLAB R2023b on an Intel(R) Xeon(R) X5680 CPU with 3.33 GHz.

A. Simulation results

Using the measurements in the simulated scenario, we calculate the mean and variance values of the scaling factor assuming a radial association for the RHM-I-KD implementations. We first transform the simulated measurement sources of the whole scenario in a local coordinate system. Afterwards, the predicted measurement sources are calculated as the intersection points of the line through the origin and the measurements with the convex hull of the CAD model. The scaling factors can then be calculated as the ratio between the simulated measurement sources and the predicted ones. The mean and variance values of the scaling factor can afterwards be calculated using standard maximum likelihood estimation.

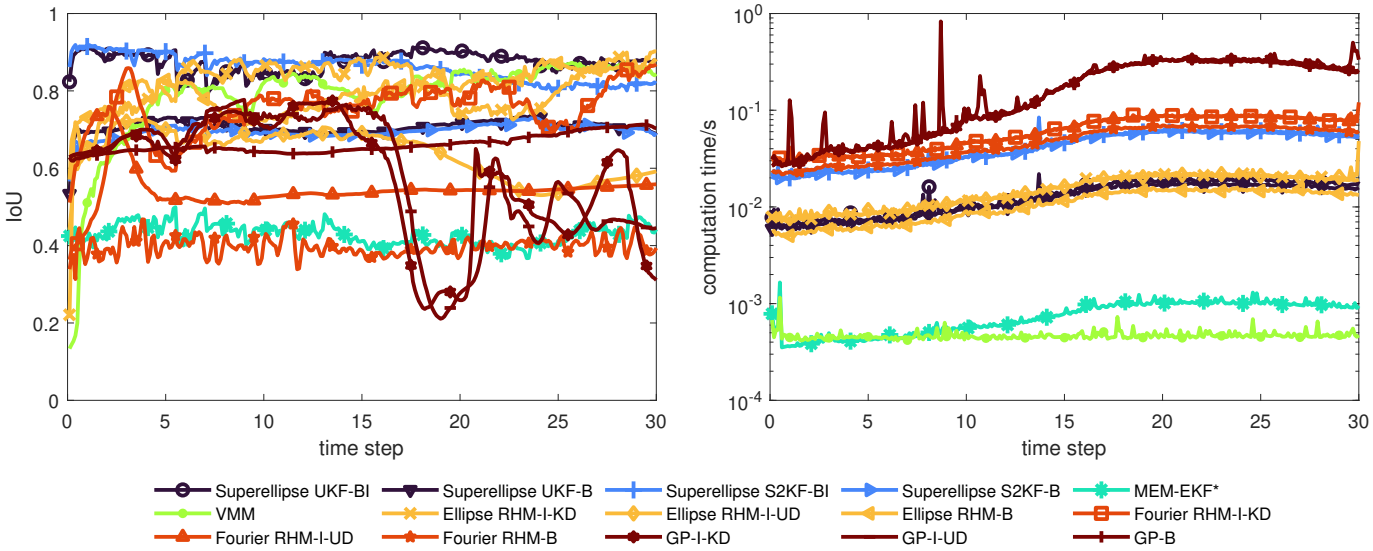

Figure 5: IoU and computation time results of the real-world scenario.

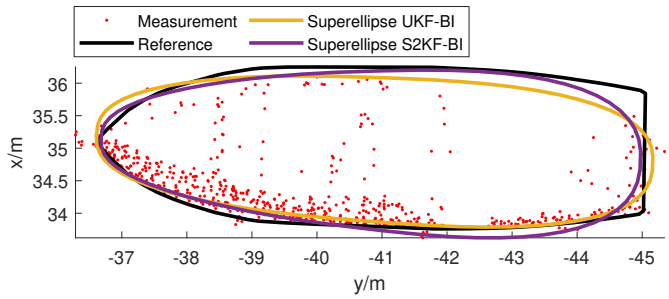

Figure 6: Exemplary results of the real-world scenario.

For the evaluation, we perform Monte Carlo (MC) simulations with 100 runs. The same trajectory is used in every run. Additionally, the simulated measurement sources are left unchanged in every run. Only the measurement noise with a standard deviation of $\sigma_{\underline{v}} = 0.1\,\mathrm{m}$ is redrawn for every measurement in every MC run. The results of the MC simulation can be seen in Fig. 4. Every curve depicts mean values over all MC runs. It turns out that the star-convex RHM with known scaling parameter distribution and the two superellipse models with recursive noise estimation show the best overall performance with respect to the IoU measure. The ellipse model with known scaling parameter distribution shows very good results as well. However, when applying a uniformly distributed squared scaling factor, the performance drastically decreases for both RHM models. Even the RHM models only assuming boundary measurements have a better performance than the implementations applying incorrectly assumed scaling factors. The MEM-EKF* also shows poor results since the assumption of uniformly spatial distributed measurements does not hold in this scenario. The VMM shows very good results and can reflect the mixed boundary-interior measurement distribution in the estimation procedure. Additionally, the VMM shows very stable computation time not depending on the number of measurements in a specific time step. The GP model with known scaling parameter distribution shows very stable results together with the highest computation in comparison. However, the performance also drastically drops when applying a uniformly distributed squared scaling factor. When comparing the computation time of the superellipse models with recursive noise estimation, the UKF implementation is considerably faster than the S2KF implementation. In future work, an improvement in the computation time for both approaches could be achieved by downsampling the measurements, which reduces the redundancy in the measurement set [32]. In total, the superellipse UKF with recursive noise estimation shows the best overall performance since the RHM implementations with known scaling parameter distribution need prior knowledge for achieving a comparable performance.

B. Real-world results

For the real-world investigation, we only evaluate a single scenario. Using an RTK-GPS on the roof of the vessel and another device attached to the stationary sensor array at the river bank, we recorded a high-precision reference pose. In combination with the CAD model, we also have a reference for the shape of the vessel. According to the sensor data sheet, we set the measurement noise standard deviation as $\sigma_{\underline{v}} = 0.025\,\mathrm{m}$ in this scenario. For the RHMs with known scaling factor distributions, we use the same mean and variance values that were calculated in the simulated scenario before. The results of the real-world scenario are depicted in Fig. 5. It can be seen that again both implementations of the superellipse model with recursive noise estimation show very good results. Also, the VMM model shows very good IoU results in combination with the lowest computation time, compared to the other approaches. In contrast, the RHM with a uniformly distributed squared scaling factor as well as the MEM-EKF* model

show poor results in comparison. The application of the better fitting scaling factor or only assuming boundary measurements drastically improves the performance of the RHM implementations. Unfortunately, the GP models applying different scaling factors both fail in this scenario. Overall, both superellipse implementations with recursive noise estimation show very good results without the need for prior knowledge. The UKF implementation again shows a faster computation time than the S2KF implementation. An exemplary shape estimate for both superellipse implementations with recursive noise estimation at a specific time step can be seen in Fig. 6. It can be seen that the deformable superellipse provides a reasonable shape approximation of the vessel and that both boundary and interior measurements can be processed using the recursive noise estimation.

VIII. Conclusion

In this paper, we proposed a measurement model for EOT using deformable superellipses as shape representation. Furthermore, we presented a recursive variance estimation procedure for an artificial measurement noise to be able to process a mixture of boundary and interior measurements. To ensure state constraints in the extent state estimate, we proposed an efficient and easy-to-implement constraining procedure in which unconstrained state estimates are transformed by transformation functions with bounded codomains. We investigated and compared our method in a simulated and real-world maritime scenario to several fixed basic parametric shape and flexible non-parametric shape-tracking models. We have seen that our approach gives the best IoU results without the need for prior knowledge.

References

[1] K. Granström and M. Baum, "A tutorial on multiple extended object tracking," *TechRxiv Preprint: https://doi.org/10.36227/techrxiv.19115858.v1*, 2022.

[2] M. Feldmann, D. Fränken, and W. Koch, "Tracking of extended objects and group targets using random matrices," *IEEE Transactions on Signal Processing*, vol. 59, no. 4, pp. 1409–1420, 2011.

[3] P. Hoher, J. Reuter, F. Govaers, and W. Koch, "Extended object tracking and shape classification using random matrices and virtual measurement models," in *2023 IEEE Symposium Sensor Data Fusion and International Conference on Multisensor Fusion and Integration (SDF-MFI)*, 2023, pp. 1–8.

[4] M. Schuster, J. Reuter, and G. Wanielik, "Multi detection joint integrated probabilistic data association using random matrices with applications to radar-based multi object tracking," *Journal of Advances in Information Fusion*, vol. 12, no. 2, pp. 175 – 188, 2017.

[5] B. Tuncer and E. Özkan, "Random matrix based extended target tracking with orientation: A new model and inference," *IEEE Transactions on Signal Processing*, vol. 69, pp. 1910–1923, 2021.

[6] M. Baum, B. Noack, and U. D. Hanebeck, "Extended object and group tracking with elliptic random hypersurface models," in *13th International Conference on Information Fusion (FUSION)*, 2010, pp. 1–8.

[7] S. Yang and M. Baum, "Tracking the orientation and axes lengths of an elliptical extended object," *IEEE Transactions on Signal Processing*, vol. 67, no. 18, pp. 4720–4729, 2019.

[8] F. Govaers, "On independent axes estimation for extended target tracking," in *2019 Sensor Data Fusion: Trends, Solutions, Applications (SDF)*, 2019, pp. 1–6.

[9] P. Broßeit, M. Rapp, N. Appenrodt, and J. Dickmann, "Probabilistic rectangular-shape estimation for extended object tracking," in *IEEE Intelligent Vehicles Symposium (IV)*, 2016, pp. 279–285.

[10] H. Kaulbersch, J. Honer, and M. Baum, "A Cartesian B-spline vehicle model for extended object tracking," in *21st International Conference on Information Fusion (FUSION)*, 2018.

[11] M. Baum and U. D. Hanebeck, "Shape tracking of extended objects and group targets with star-convex RHMs," in *14th International Conference on Information Fusion (FUSION)*, 2011.

[12] N. Wahlström and E. Özkan, "Extended target tracking using Gaussian processes," *IEEE Transactions on Signal Processing*, vol. 63, no. 16, pp. 4165–4178, 2015.

[13] H. Alqaderi, F. Govaers, and W. Koch, "Bayesian Wishart filter for random shape tracking," *IEEE Transactions on Aerospace and Electronic Systems*, vol. 58, no. 3, pp. 1941–1952, 2022.

[14] B. Tuncer, U. Orguner, and E. Özkan, "Multi-ellipsoidal extended target tracking with variational Bayes inference," *IEEE Transactions on Signal Processing*, vol. 70, pp. 3921–3934, 2022.

[15] P. Rosin, "Fitting superellipses," *IEEE Transactions on Pattern Analysis and Machine Intelligence*, vol. 22, no. 7, pp. 726–732, 2000.

[16] L. A. Giefer and J. Clemens, "State estimation of articulated vehicles using deformed superellipses," in *2021 IEEE 24th International Conference on Information Fusion (FUSION)*, 2021, pp. 1–8.

[17] R. Pascoal, V. Santos, C. Premebida, and U. Nunes, "Simultaneous segmentation and superquadrics fitting in laser-range data," *IEEE Transactions on Vehicular Technology*, vol. 64, no. 2, pp. 441–452, 2015.

[18] H. Kaulbersch, J. Honer, and M. Baum, "Assymetric noise tailoring for vehicle lidar data in extended object tracking," in *2020 IEEE International Conference on Multisensor Fusion and Integration for Intelligent Systems (MFI)*, 2020, pp. 191–196.

[19] Y. Xia, P. Wang, K. Berntorp, L. Svensson, K. Granström, H. Mansour, P. Boufounos, and P. V. Orlik, "Learning-based extended object tracking using hierarchical truncation measurement model with automotive radar," *IEEE Journal of Selected Topics in Signal Processing*, vol. 15, no. 4, pp. 1013–1029, 2021.

[20] E. Dura, J. Bell, and D. Lane, "Superellipse fitting for the recovery and classification of mine-like shapes in sidescan sonar images," *IEEE Journal of Oceanic Engineering*, vol. 33, no. 4, pp. 434–444, 2008.

[21] F. Solina and R. Bajcsy, "Recovery of parametric models from range images: The case for superquadrics with global deformations," *IEEE Transactions on Pattern Analysis and Machine Intelligence*, vol. 12, no. 2, pp. 131–147, 1990.

[22] A. Zea, F. Faion, M. Baum, and U. D. Hanebeck, "Level-set random hypersurface models for tracking nonconvex extended objects," *IEEE Transactions on Aerospace and Electronic Systems*, vol. 52, no. 6, pp. 2990–3007, 2016.

[23] P. Hoher, T. Baur, J. Reuter, F. Govaers, and W. Koch, "A circular detection driven adaptive birth density for multi-object tracking with sets of trajectories," in *2022 25th International Conference on Information Fusion (FUSION)*, 2022, pp. 1–8.

[24] E. Wan and R. Van Der Merwe, "The unscented Kalman filter for nonlinear estimation," in *Proceedings of the IEEE 2000 Adaptive Systems for Signal Processing, Communications, and Control Symposium (Cat. No.00EX373)*, 2000, pp. 153–158.

[25] J. Steinbring and U. D. Hanebeck, "LRKF revisited: The smart sampling Kalman filter (S2KF)," *Journal of Advances in Information Fusion*, vol. 9, no. 2, pp. 106–123, 2014.

[26] F. Faion, M. Baum, and U. D. Hanebeck, "Tracking 3D shapes in noisy point clouds with random hypersurface models," in *15th International Conference on Information Fusion (FUSION)*, 2012, pp. 2230–2235.

[27] B. O. Teixeira, L. A. Tôrres, L. A. Aguirre, and D. S. Bernstein, "On unscented Kalman filtering with state interval constraints," *Journal of Process Control*, vol. 20, no. 1, pp. 45–57, 2010.

[28] T. Baur, J. Reuter, A. Zea, and U. D. Hanebeck, "Shape tracking using Fourier-Chebyshev double series for 3D distance measurements," in *2023 26th International Conference on Information Fusion (FUSION)*, 2023, pp. 1–8.

[29] *Alpha Prime Powering Safe Autonomy*, Velodyne Lidar, 2019, Rev. 1.

[30] M. Roth, G. Hendeby, and F. Gustafsson, "EKF/UKF maneuvering target tracking using coordinated turn models with polar/Cartesian velocity," in *17th International Conference on Information Fusion (FUSION)*, 2014.

[31] M. Levandowsky and D. Winter, "Distance between sets," *Nature*, vol. 234, pp. 34–35, 1971.

[32] T. Baur, J. Reuter, and U. D. Hanebeck, "On runtime reduction in 3D extended object tracking by measurement downsampling," in *2023 IEEE Symposium Sensor Data Fusion and International Conference on Multisensor Fusion and Integration (SDF-MFI)*, 2023, pp. 1–6.